Open Ceramics 17 (2024) 100519

Contents lists available at ScienceDirect

Open Ceramics

journal homepage: www.sciencedirect.com/journal/open-ceramics

Lanthanide element variation in rare earth doped ceria – $FeCo_2O_4$ dual phase oxygen transport membranes

Liudmila Fischer [a,b,*], Ke Ran [c,d], Christina Schmidt [e], Kerstin Neuhaus [e], Stefan Baumann [a,**], Patrick Behr [a], Joachim Mayer [c,d], Henny J.M. Bouwmeester [b], Arian Nijmeijer [b], Olivier Guillon [a,f], Wilhelm A. Meulenberg [a,b]

[a] Institute of Energy and Climate Research IEK-1, Forschungszentrum Jülich GmbH, 52425, Jülich, Germany
[b] Faculty of Science and Technology, Inorganic Membranes, University of Twente, 7500 AE, Enschede, the Netherlands
[c] Central Facility for Electron Microscopy GFE, RWTH Aachen University, 52074, Aachen, Germany
[d] Ernst Ruska-Centre for Microscopy and Spectroscopy with Electrons ER-C, Forschungszentrum Jülich GmbH, 52425, Jülich, Germany
[e] Forschungszentrum Jülich GmbH, Institute of Energy and Climate Research IEK-12, Helmholtz-Institute Münster, 48149, Münster, Germany
[f] Jülich Aachen Research Alliance: JARA-Energy, 52425, Jülich, Germany

ARTICLE INFO

Handling Editor: Dr P Colombo

Keywords:
Ceria-based somposites
Mixed ionic-electronic conductors
Dual phase oxygen transport membrane
Ceramic materials
Optimization
Microstructure
Doped-ceria
Spinel-type ferrite
Oxygen permeation

ABSTRACT

The increased interest in dual-phase membrane materials for oxygen separation leads to the continuous optimization of their composition. Rare-earth doped ceria is a promising candidate as the ion-conducting phase in the membrane. Spinel-structured $FeCo_2O_4$ was investigated as an electronic conducting phase forming an additional electronic conducting perovskite-structured phase during sintering when combined with Ce1−xLnxO2−δ. The influence of rare-earth lanthanide elements, i.e., Gd and Sm, as well as their concentration, i.e. x = 0.1 and 0.2, on the final phase composition and microstructure as well as its related functional properties in particular oxygen permeation is analyzed. 20 mol.% doping of either Gd or Sm reveals a multi-phase microstructure after sintering. Moreover, segregation of Gd/Sm, iron, and cobalt is found at the ceria-ceria grain boundaries in $Ce_{0.8}Sm_{0.2}O_{2-\delta}$- and $Ce_{0.9}Gd_{0.1}O_{2-\delta}$-based composites. In contrast, 10 mol.% Gd–doping leads to a dual-phase membrane material without the formation of any other phase. In all cases, the percolation threshold is reached at approx. 20 vol% of the electron-conducting phase in the system leading to similar maximum permeation rates determined by the ionic conductivity of the ceria phase.

1. Introduction

Oxygen is an important gas for various technical applications such as combustion processes, partial oxidations in the chemical industry, or medical applications. Although oxygen is freely available in the air, its separation is a complex and energy-consuming process. Due to lower energy demand, ceramic membranes offer a good alternative to other known gas separation methods, such as cryogenic distillation, reducing operation costs and energy consumption [1–4]. These ceramic membranes consist of mixed ionic–electronic conducting (MIEC) oxides [5–7]. At high temperatures (typically 850–950 °C), these MIECs show high oxygen permeation involving both oxygen ionic conductivity and electronic conductivity.

There are several known Oxygen transport membrane (OTM) materials with high oxygen flux, e.g., $Ba_{0.5}Sr_{0.5}Co_{0.8}Fe_{0.2}O_{3-\delta}$ and $La_{0.6}Sr_{0.4}Co_{0.2}Fe_{0.8}O_{3-\delta}$, [8–11]. However, these single-phase materials suffer from limited mechanical and chemical stability, especially under acidic (e.g. CO_2, SO_x) or reducing (e.g. H_2, CO) conditions, which makes them low performing in numerous industrial applications [12–17]. Therefore, dual-phase material systems, utilizing two inherently stable ionic- and electronic-conducting phases, have again attracted attention from the scientific community [1,5,6]. Nowadays, dual- and multiphase membranes with separate ionic and electronic conductors are among the most promising materials regarding stability for the application in membrane reactors [18].

The dual-phase $Ce_{0.8}Gd_{0.2}O_{2-\delta}$ –$FeCo_2O_4$ (CGO20-FCO) composite has been previously investigated in the context of the microstructure design and structural properties, mechanical properties as well as

* Corresponding author. Institute of Energy and Climate Research IEK-1, Forschungszentrum Jülich GmbH, 52425, Jülich, Germany.
** Corresponding author.
E-mail address: li.fischer@fz-juelich.de (L. Fischer).

https://doi.org/10.1016/j.oceram.2023.100519
Received 13 July 2023; Received in revised form 27 November 2023; Accepted 30 November 2023
Available online 4 December 2023

permeation performance and showed to be a good candidate for application in a membrane reactor at intermediate temperatures (<800 °C) [19,20]. It was estimated that during the phase interaction, approximately 10 mol. % of gadolinium remains in the ion-conductive fluorite phase [21,22] the remainder is used for perovskite phase formation, which is an additional electron conductor. The ionic conductivity is still the limiting factor in this material, thus the investigated doping content of the rare earth-lanthanide element in the fluorite system Ce1−xLnxO2−δ can be narrowed to a range of 10–20 mol.%, where the fluorite structure is stable [23,24]. Within the family of Ln-doped ceria, Gd- and Sm-doped systems are the most efficient, so the these doped ceria are the most prominent candidates due to their good chemical stability [25–29] and excellent ionic conductivities (~0.075–0.1 S·cm−1) [30–35].

According to the literature, the ionic conductivities of 10 mol.% Gd-doped ceria (CGO10) or 20 mol% Sm-doped ceria (CSO20) are higher than the previously investigated CGO20 and, thus, are good candidates as ceria-FCO composites [36]. Comparison of the modeled conductivity of the rare-earth doped ceria at 500 °C reveals that the Sm-doped material has the highest ionic conductivity at approximately 10 mol.% of samarium [37]. In those calculations, apart from the acceptor dopant concentration also the interaction between dopant cations and mobile oxygen vacancies is taken into account [35,37]. Koettgen et al. [37] performed Kinetic Monte Carlo simulations (KMC) at 400 °C, suggesting that 10 mol% Gd-doped ceria has a higher ionic conductivity compared to 20 mol.% Gd-doped ceria. This is assigned to a larger oxygen ion mobility in the CGO10 material, whereas the high ionic conductivity in CGO20 is reached due to the higher concentration of oxygen vacancies [38–40].

The computed ionic conductivity of neodymium and samarium doped ceria is even higher compared to the gadolinium doped ceria at 400 °C [35]. Neodymium on the other hand is regarded as critical within RE-elements mainly due to its importance in permanent magnets [41]. Therefore, it is not considered in this study.

The experimental data at 600 °C shows that both, gadolinium and samarium doping, leads to a plateau in the total ionic conductivity between approximately 10-20 mol.% dopant, as discussed by Koettgen et al. [37]. That makes both dopants really attractive for the ceria materials. Moreover, the resulting permeation performance of a dual- or multi-phase composite membrane is not only dependent on the individual conductivities of the single phases, but bulk and grain boundary contributions to the conductivity could also be affected by e.g., phase interactions.

The grain boundaries in the doped-ceria ceramics can be highly resistive and serve as a barrier to oxygen ion transport across them. Avila Paredes et al. [42] reported that the activation energy E_a of the grain boundary conductivity decreases with decreasing dopant concentration in the fluorite. As a summary, the higher lattice conductivity and lower grain boundary resistance makes CGO10 more appropriate for application at intermediate temperatures [43]. Moreover 10 mol. % doped ceria shows better stability in reducing atmospheres compared to CGO20 [29,44].

Therefore, in this study we investigate the phase interactions of CGO10 and CSO20 with $FeCo_2O_4$ in comparison to formerly reported CGO20 [19]. Composite membranes were synthesized by solid state reactive sintering in varying weight ratios. The resulting phase composition and microstructure as well as functional properties are analyzed and its relationships are discussed.

2. Experimental

2.1. Samples fabrication

Commercially available $Ce_{0.9}Gd_{0.1}O_{2-\delta}$ (CGO10) (Solvay), $Ce_{0.8}Sm_{0.2}O_{2-\delta}$ (CSO20) (Kceracell), Fe_2O_3 (FO) (Merck, 99 %) and Co_3O_4 (CO) (Merck, 99 %) powders were synthesized by Solid-State Reactive Sintering method (SSRS). Respective amounts of powders were weighted for nominal CGO10-FCO and CSO20–FCO compositions with wt. % -ratios 60:40, 70:30, 80:20, 85:15, and 90:10. During 48 h the powder mixtures were ball-milled on a roller bench with a speed of 175 rpm. After drying in ambient air at 70 °C for 48 h powder mixtures were pressed with a uniaxial press in disc-shaped membranes with d = 20 mm and sintered at 1200 °C for 5 h in air with the heating rate 5 K min^{-1}. At sintering temperature, the spinel partially reduces into a high-temperature monoxide phase with a rock salt structure. To ensure complete reoxidation of the high-temperature Co/Fe-monoxide phase to the spinel phase stable at operating temperatures according to the $Fe_{3-x}Co_xO_4$ phase diagram a slow rate of 0.5 K min^{-1} between 900 and 800 °C is implemented in the cooling cycle. The membranes are considered to be sufficiently dense to exclude leakage since the leaked oxygen flux calculated from the nitrogen leak rate is low. After the sintering step, all samples were ground down to 1 mm-thick discs in 2 steps applying SiC merge papers with different grits from P 800 to P 1200 (by WS FLEX 18C). On both sides of the discs a porous $La_{0.58}Sr_{0.4}Co_{0.2}Fe_{0.8}O_{3-\delta}$ (LSCF) catalytic activation layer with a thickness of ~5 μm was applied via a screen-printing technique and the final membrane was calcined in an oven at 1100 °C for 5 h.

2.2. Characterization methods

2.2.1. Crystal structure

The X-ray diffraction (XRD) diffractometer D4 ENDEAVOR (Bruker, Germany) is exploited for crystal structure determination. The diffraction angle 2θ is in the range from 10° to 80°, with increments of 0.02° 2θ and 0.75 s of measurement time per step. Measured data is analyzed with the help of the program package X'Pert HighScore (PANalytical B. V., version 3.0.5) software. Crystal structure analysis and associated phase quantifications were carried out by Rietveld refinement using the software Profex (Version 4.2.2). The errors of each fit are calculated individually and given in Tables 1 and 2.

2.2.2. Microscopy

To obtain material morphology Scanning Electron Microscopy (SEM) and Energy Dispersive X-ray Spectroscopy (EDXS) were used. SEM images were taken with a Zeiss Ultra 55 and a Zeiss Supra 50 VP1 (Carl Zeiss NTS GmbH, German) SEM at different magnifications. The electronic conductivity of the samples was enhanced by sputter deposition of a thin platinum layer prior to the SEM measurement.

Further image analysis-based method was conducted via ImageJ software on all composite samples including ~1000 grains utilizing so-called isodata threshold method [45], which helped to estimate the average grain size of all phases as well as area fraction of pores. However, the limited number of characterized grains/pores might induce large inaccuracy in the grain size and pore size calculations.

The Transmission Electron Microscopy (TEM) characterization was also performed on both investigated materials. All specimens were cut from sintered composite pellets by Focused Ion Beam (FIB) milling using an FEI Strata 400 system with a gallium ion beam. Further thinning and cleaning was done by using an argon ion beam in a Fischione Nanomill 1040 at beam energies of 900 eV and 500 eV. TEM and energy-filtered TEM (EFTEM) imaging was performed using an FEI Tecnai F20 at 200 kV. The FEI Titan G2 80–200 ChemiSTEM microscope equipped with an XFEG and a probe Cs corrector was used in order to obtain high-resolution high-angle annular dark-field (HAADF) images and EDXS chemical mapping [46].

2.2.3. Electrical conductivity

The total conductivity of the single-phase fluorite samples was determined by analyzing the temperature-dependent impedance spectra with the help of a Novotherm HT 1200 frequency analyzer. All samples were coated with a Pt resinate paste (RP 070107, Heraeus GmbH, Germany) and on both sides of the sample Pt sheet contacts were attached

Table 1
Lattice parameter and fraction (F) of the phases after quantification by Rietveld refinement analyses of the CSO20–FCO composites and single CSO phase sintered at 1200 °C for 5 h.

FCO, %	CSO *Fd3m*		FCO *Fd3m*		Co_3O_4 *Fd3m*		CSFCO *Pnma*			
	F, wt.%	a = b = c, Å	F wt.%	a = b = c, Å	F, wt.%	a = b = c, Å	F, wt.%	Lattice parameter, Å		
								a	b	c
0	100	5.4314 [4]	–	–	–	–	–	–	–	–
10	80.24[73	5.426 [6]	0	#	10.95 [6]	8.152 [2]	8.81 [7]	5.381 [4]	5.597 [6]	7.691 [7]
15	76.94 [9]	5.425 [4]	0.65 [7]	8.312 [1]	15.3 [1]	8.174 [3]	7.15 [3]	5.385 [5]	5.601 [5]	7.696 [6]
20	71.70 [4]	5.425 [7]	5.81 [4]	8.312 [9]	16.22 [7]	8.156 [2]	6.27 [2]	5.385 [4]	5.60 [4]	7.697 [8]
30	63.46 [9]	5.424 [5]	8.31 [3]	8.312 [3]	22.7 [2]	8.182 [5]	5.52 [3]	5.383 [7]	5.601 [3]	7.698 [1]
40	51.57 [8]	5.421 [8]	16.96 [9]	8.298 [8]	25.90 [4]	8.149 [1]	5.55 [4]	5.378 [9]	5.598 [8]	7.691 [6]

Table 2
Lattice parameter and fraction (F) of the phases after quantification by Rietveld refinement analyses of the CGO10-FCO composites and CGO10 singe phase sintered at 1200 °C for 5 h.

FCO, %	CGO, *Fd3m*		FCO, *Fd3m*		Co_3O_4, *Fd3m*	
	F, wt.%	a = b = c, Å	F wt.%	a = b = c, Å	F, wt.%	a = b = c, Å
0	100.0 [0]	5.4172[7]	–	–	–	–
10	89.80 [1]	5.4175[3]	8.07[5]	8.326[8]	2.14[9]	8.1456[3]
15	84.95 [8]	5.4173[9]	7.62[8]	8.306[1]	7.43[6]	8.1467[8]
20	79.04 [2]	5.4179[1]	14.12 [2]	8.303[6]	6.84[2]	8.1457[1]
30	69.18 [4]	5.4172[3]	16.07 [1]	8.304[2]	14.75 [9]	8.1460[0]
40	58.51 [4]	5.4179[6]	22.53 [3]	8.299[2]	18.29 [3]	8.1351[4]

and measured in air. For all measurements an AC voltage peak-to-peak amplitude of 40 mV was applied. As the electronic conductivity of both spinels was very high, no division into separate contributions from the grain bulk and grain boundary was visible. Nyquist plots instead only showed a straight line (ohmic contribution from electron conducting phase).

2.2.4. Oxygen permeation measurements

All composite materials were subjected to oxygen permeation experiments. The experimental setup consisted of vertical quartz glass housing, where the membrane pellets were sealed with two gold rings with an inner diameter of 13 mm. The separation of the oxygen from ambient air fed with 250 $ml_N\ min^{-1}$ was performed in a temperature range between 650 °C and 1000 °C. As a sweep gas argon was used with 50 $ml_N\ min^{-1}$ flow rate using mass flow controllers (Bronkhorst, Germany). The mass spectrometer (Omnistar, Pfeiffer Vacuum GmbH, Germany) detected concentrations of oxygen and nitrogen in the permeate gas, i.e. oxygen enriched argon. With help of measured nitrogen concentration, air leakage through either membrane or the sealing was calculated according to

$$j_{O_2} = F_{Ar}\left(\frac{X_{O_2} - \frac{1}{4}X_{N_2}}{1 - X_{O_2} - X_{N_2}}\right)\frac{1}{A_{mem}} \qquad \text{Equation 1}$$

Here F_{Ar} is the argon flow rate, *i.e.* 50 $ml_N\ min^{-1}$, X_{O2} and X_{N2} the oxygen and nitrogen concentration in the permeate gas, respectively, and open membrane area is $A_{mem} = 1.33\ mm^2$. The factor $\frac{1}{4}$ reflects the O_2/N_2 ratio in the air feed assuming that the leak is not gas selective.

Since the oxygen partial pressure in the permeate gas is temperature dependent, the driving force of the permeation rate is not constant during the measurement. Additionally, the sample thickness deviation after the grinding process was ±8 % from the target thickness of 1 mm. Consequently, the driving force normalized permeation rate, also referred to as permeance, was normalized to the reference thickness of $L_0 = 1$ mm and was calculated assuming Wagner behavior using the following equation.

$$Permeance = \frac{j_{O_2}}{ln\frac{p'_{O_2}}{p''_{O_2}}\frac{L_{mem}}{L_0}} \qquad \text{Equation 2}$$

Here, p'_{O_2} and p''_{O_2} are the oxygen partial pressures in the retentate and permeate gas, respectively, and L_{mem} is the actual membrane thickness. The overall experimental error is assumed to be ±10 %, which is well accepted in the literature.

3. Results and discussion

3.1. Microstructure evolution

3.1.1. CSO20–FCO composite

Compositional and structural characterization is carried out for pellets with nominal composition of (100-x) wt.% $Ce_{0.8}Sm_{0.2}O_{1.9}$ (CSO20) and x wt.% $FeCo_2O_4$ (FCO), where $10 \leq x \leq 40$. X-ray diffraction confirmed that during the sintering process, several phase interactions take place resulting in the mixture of three structures: CSO with a cubic fluorite structure, $Fe_{3-x}Co_xO_4$ with a cubic spinel structure, and $SmFeO_3$ with an orthorhombic perovskite structure as shown in Fig. 1. The intensities of the spinel reflections are increasing with the increase of the nominal FCO amount in the composite. This is an identical result compared to the 20 mol.% Gd-doped ceria (CGO20) composite, where the formation of the tertiary perovskite phase was also reported [19]. However, there are reports for the CSO20-based composite addressing to the third phase formation, depending on the type of added spinel and preparation methods [47,48]. Similarly to the CGO20-based composites and with respect to the Fe–Co oxide phase diagram: there are two spinel phases in equilibrium, i.e., iron-rich (inverse spinel) and cobalt-rich (normal spinel) [49]. Both are present in all CSO20-based composites, except for the 90:10 ratio, where only the normal spinel phase (Co_3O_4) is observed. Probably, most of the iron is consumed by the perovskite formation, so that the remaining Fe/Co-ratio decreases and only normal spinel forms accordingly.

Subsequent Rietveld refinement quantified the composition of CSO20-based composites, listed in Table 1. The lattice parameter of the CSO20 phase measured before phase interaction is a = 5.4314 Å and decreases with increasing addition of FCO, as for CGO20-based composite [19]. Since the solubility of iron and cobalt in ceria is very limited (approx. 1–2 %) [50–53] this decrease in the lattice constant is accounted to the extraction of Sm from the ceria lattice forming the tertiary $SmFeO_3$-based perovskite phase during sintering (where Sm takes the A sites in the formed ABO_3 phase structure, while for the B sites iron cations are more favorable). In analogy to the CGO20 composite Ce

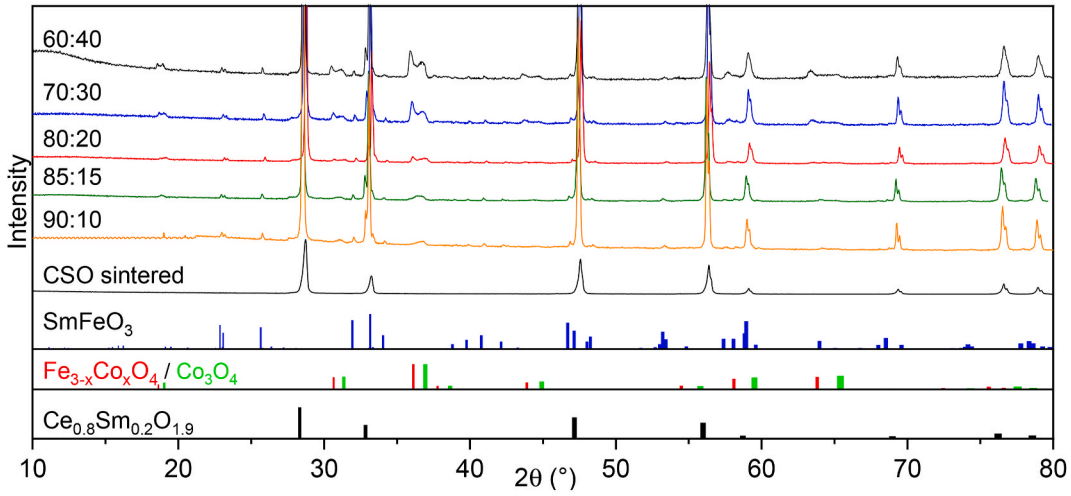

Fig. 1. XRD pattern of CSO20–FCO composites and CSO20 single phase sintered at 1200 °C for 5 h as well as three main defined phases.

and Co are partly occupying the A- and B-site, respectively, resulting in the formula $(SmCe)(FeCo)O_3$ (SCFCO).

The composition of individual phases is estimated via empirical models similarly to the analysis performed on the CGO20-FC2O composite, described in Ref. [19]. About 10 mol % of Sm forms the tertiary phase during the sintering process, resulting in the residual 10 mol % of Sm in CSO phase, what is similar to the CGO20-based composite.

SEM analysis shows the homogeneous distribution of these phases (Fig. 2a). Three phases can be distinguished in different grey scale due to the material contrast (different average atom number) detecting back scattered electrons, Fig. 2b. The image analysis, conducted on all CSO20-based samples including more than 1000 grains, revealed a mean grain size in the range of 0.5–0.85 μm.

Further TEM analysis accompanied by energy-filtered (EFTEM) elemental mapping confirmed fluorite, spinel, and perovskite phases in all CSO20–FCO samples. The distribution of the three phases in the composite 60CSO20–FCO reveal a presence of perovskite grains. According to the EFTEM elemental mapping, the iron and cobalt show a non-uniform distribution in the FCO phase hence it can be subdivided into two spinel types: normal cobalt-rich and an inverse iron-rich spinel. This agrees well with the XRD analyses the phase diagram predicting two coexisting spinel phases.

The presence of the aforementioned three phases gives a feasibility to observe six interfaces, which might contribute to different types of transport within the composite material. The spinel and perovskite grains form a connected chain, which is responsible for the e-transport, while CGO grains enable ionic transport. The analysis of the interfaces by HAADF imaging is shown in Fig. 3 for the 60CSO20–FCO composite. Most of the grain boundaries are clean without any visible defects or precipitations. Generally, defects and disordered features along the interfaces are not desired and quite unfavorable for any membrane materials, since they could strongly affect both types of conductivities. Thus, there are no barriers that significantly hinder or facilitate the transport of the oxygen ions or electrons/holes either via or across the grain boundaries.

Fig. 3c shows further EDX mapping in atomic scale, confirming that our results are fitting the best with the $SmFeO_3$-based perovskite, which indeed contains cerium and cobalt at the A- and B-site, respectively. The oxygen atoms are placed between the cation columns and are not visible by HAADF imaging, due to much smaller atomic number than cerium and samarium.

A closer look was taken to the ceria-ceria interface, Fig. 4, at which often element segregation occurs [20]. Line scans along the blue arrow are plotted in Fig. 4b. A clear enrichment of samarium, iron and cobalt and a significant loss of cerium along the CSO–CSO grain boundary is visible. This has been already previously reported in similar CGO20-based membranes, where the $GdFeO_3$-phase is predominately surrounded by ceria grains [54]. Therefore, these segregations might be an early stage of the formation of an emerging perovskite-phase in both composites.

Similar, to the CGO an excess of oxygen vacancies and samarium is expected in the grain boundary core. As can be seen, the concentration of samarium is much higher along the grain boundaries than samarium concentration in the grain.

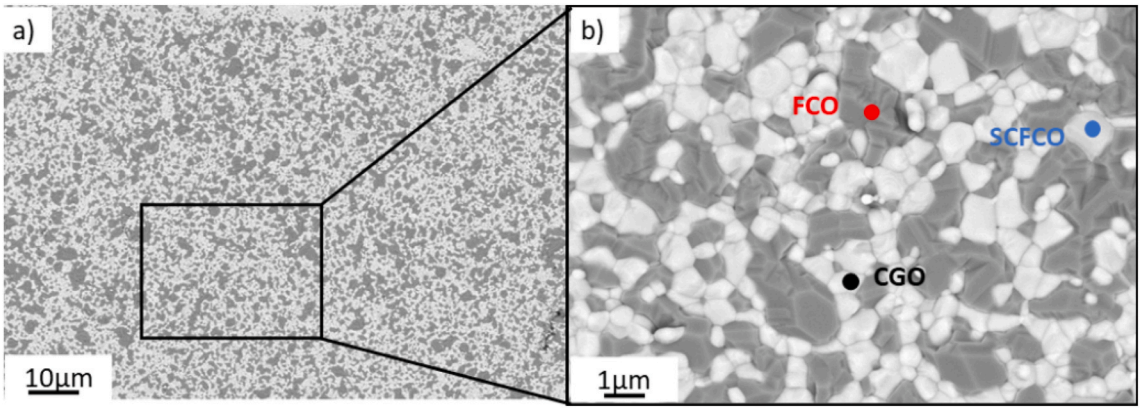

Fig. 2. SEM image of the surface of 60CSO20–FCO sample sintered at 1200 °C for 5 h with marked fluorite (light), spinel (black) grains, and perovskite (grey).

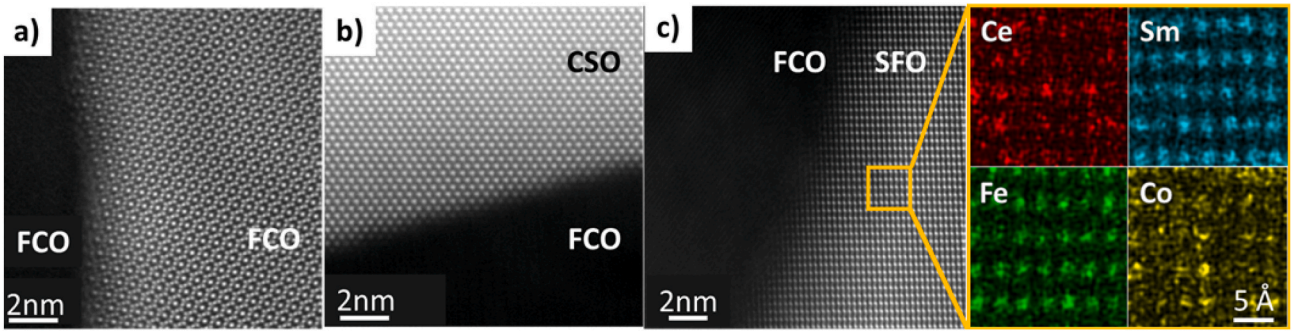

Fig. 3. HAADF image of grain boundaries between phases in the 60CSO20–FCO system (a) FCO– FCO; (b) CSO–FCO; (c) FCO-SFO inclusive the EDX chemical mapping of perovskite grain along [010].

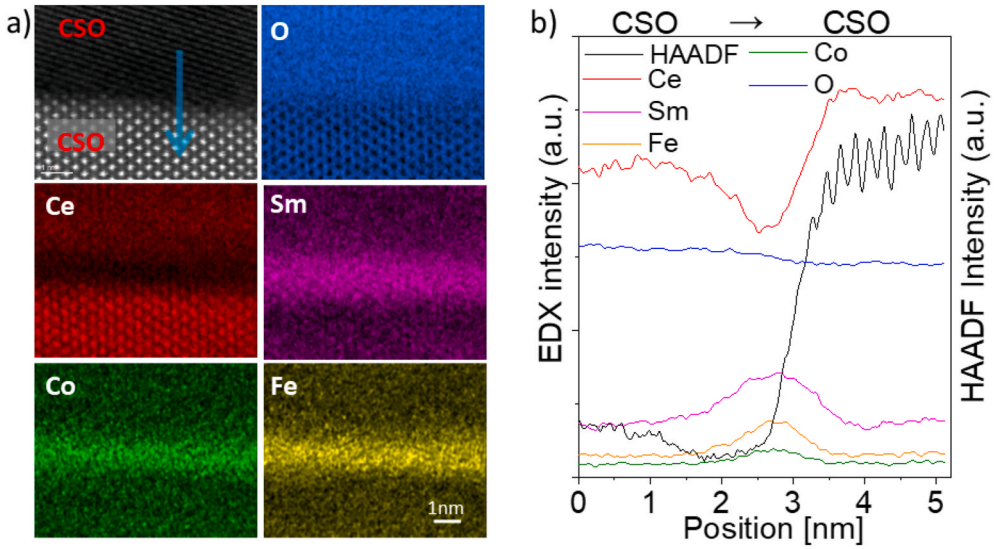

Fig. 4. EDXS analysis of a ceria-ceria grain boundary in 60CSO20–FCO a) The simultaneously acquired HAADF image and EDXS chemical mapping from Ce L, Sm L, Fe K, Co K, and O K peak. b) Line scans between two fluorite grains marked as CSO grains based on the elemental maps.

3.1.2. *CGO10-FCO composite*

Compositional and structural characterization is carried out for pellets with nominal composition of (1-x) wt.% CGO10 - x wt. % FCO, where $10 \leq x \leq 40$. XRD patterns in Fig. 5 confirmed the presence of a cubic fluorite phase, i.e., ceria, and cubic spinel-type phases, i.e., Co_3O_4 and $Fe_xCo_{3-x}O_4$. Again, there is a coexistence of the two spinel types in all CGO10-based composites. The increase of the spinel reflections in the region of $35 \leq 2\theta \leq 38°$ and approximately $63°2\theta$ with increasing nominal spinel fraction in the initial composite can nicely be observed. However, no additional $GdFeO_3$ perovskite phase can be detected. In contrast to composites with CGO20 or CSO20, there is no phase interaction during the sintering process, thus indeed a dual-phase membrane

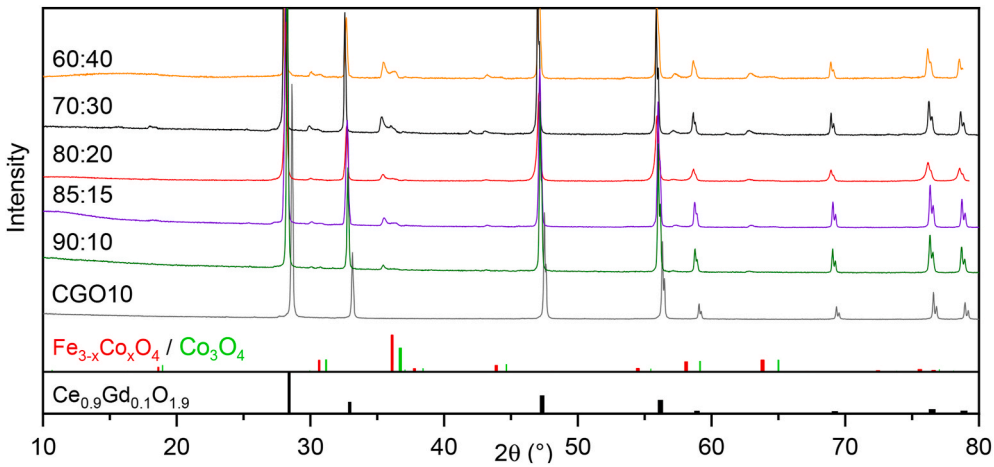

Fig. 5. The XRD patterns of CGO10-FCO materials sintered at 1200 °C for 5 h and single phase CGO10 as well as peak positions of phases.

material is achieved.

Further Rietveld refinement quantified the weight fractions of each phase as shown in Table 2. The resulting amount of fluorite fraction is reduced in each sintered composite compared to the nominal CGO10 content in the initial powder mixture. The lattice parameter of pure CGO10 measured in this work is 5.4172 Å agreeing well with literature reporting 5.418–5.42 Å [55,56]. In the composites, the lattice parameter of CGO10 is found to remain relatively constant after sintering confirming that no significant gadolinium extraction. For comparison in CGO20-based compounds the lattice parameter reduces by approx. 0.12 ± 0.02 %% due to the loss in gadolinium, which is consumed during the perovskite phase formation.

SEM analysis confirmed the presence of two phases in CGO10 –FCO composites: fluorite (light grains), and spinel (dark grains), without any other detectable phase. The grains are closely packed and uniformly distributed, exemplarily shown for 60:40 wt%-ratio in Fig. 6. The visual microstructure analysis of both surface and cross-section images via ImageJ software reveals the homogeneous distribution of the phases with a mean grain size of 0.5 μm. The spinel grains, in general, are larger than fluorite grains in both composites.

Image analysis was conducted on all samples of CGO10-, CGO20- and CSO20-based composites of both cross-section and surface images [57]. The average grain and pore sizes are given in Fig. 7. The relationship between the dopant amount and grain size distribution in composites is seen by detailed analysis, included more than 2000 grains. The mean grain size of the two composites and reference CGO20-based composite is lying in the range of 0.5–0.68 μm and slightly increases with the higher dopant concentration. Both 20 mol.% doped composites reveal almost the same mean grain size, which is larger compared to 10 mol.% Gd-doped ceria. This result is logical since CGO10 powder was much finer, compared to 20 mol.% doped ceria. The grain growth is inhomogeneous in CGO20 and CSO20 composites, while in CGO10 composite all grains have similar size. In 20 mol%-doped composite FCO grains are larger compared to the other phases, as can be seen in Fig. 7a. The porosity percentages have been estimated from the SEM images via image analysis, while the relative density was estimated geometrically from the dimensions and weight of the as-sintered pellets. The resulting values of both methods are well in agreement, Fig. 7b. The dopant seems to have no significant effect on the grain and pore sizes, however the amount of the dopant (10 or 20 mol.%) seems to make a difference. Both CSO20 and CGO10-based composites reveal high level of relative density (>95–97 %) and correspondingly very low level of porosity (~1–2 %), these parameters are improved compared to the reference CGO20-FCO composite.

TEM analysis of the 10 and 20 mol. % Gd doped ceria composites reveal uniformly distributed element maps, as illustrated in Fig. 8. Taking a closer look, a difference can be noticed in the Gd map: CGO10 has an evenly distributed intensity in composite, free of any tertiary phase, while the several grains are revealed with the higher gadolinium intensity in the CGO20-based sample, which confirms the presence of the perovskite phase in the microstructure.

The HAADF image and EDXS chemical mapping in Fig. 9 contain a CGO GB in the 60CGO10-FCO composite G1 and G2. Both fluorite grains are randomly oriented. G1 appears brighter in the HAADF image as well as in the elemental maps most likely because it is closer to a zone axis compared to G2. As indicated by the blue arrow, intensity profiles across the grain boundary were extracted and plotted in Fig. 9b.

Along the grain boundary, the enrichment of the gadolinium together with the migrated iron and cobalt was detected, while the Ce is significantly depleted. In addition, a slight depletion in oxygen, i.e., segregation of oxygen vacancies, can be observed. This is in agreement with literature about pure Gd-doped ceria, where excess of Gd^{3+} and depletion of oxygen ions in the grain boundary core appears, what can be also considered as an accumulation of the oxygen vacancies [54,58,59]. Compared to the CGO20 and CSO20 composites, the segregation of the gadolinium in CGO10 composite is less pronounced, which can be attributed to the initial amount of the gadolinium in the fluorite [60]. Additionally, an excess of electrons near the grain boundary can be expected, as reported by Lei et al. [61].

The formed perovskite grains in the CGO20-FCO composites are mainly found between the fluorite grains [19,60]. In contrast, the initial gadolinium would be insufficient in CGO10-FCO, which possibly hinders the formation of a perovskite phase and often leaves iron and cobalt segregation along the fluorite-fluorite grain boundaries. Therefore, the segregation of iron and cobalt in the grain boundary of CGO10-based composites might also indicate a very initial stage of perovskite phase formation, which remains incomplete because of too low availability of gadolinium.

Summarizing, in CGO10 the gadolinium appears very strongly bound in the ceria lattice, whereas the excess amount of gadolinium in CGO20 (as well as samarium in CSO20) can be extracted by Fe/Co-oxides forming the perovskite phase. The lattice parameter of pure CGO20 and CSO20 prior to phase interaction was 0.54246 nm and 0.54314 nm, respectively, and it was found to decrease after phase interaction due to Gd/Sm extraction. The residual doping content in the fluorite phase of the sintered composites was calculated from the lattice parameter, and shown in Fig. 10. In the case of the CGO10-FCO composite, the amount of gadolinium is initially lower compared to the CGO20-FCO gadolinium content in the system. This shows the influence of the initial gadolinium content in the composite on the formation of the emerging perovskite phase. All composites end up at a dopant content of approx. 10 mol.% in the ceria phase.

3.2. Functional properties

Fig. 11 shows the total conductivity of single-phase ceria materials

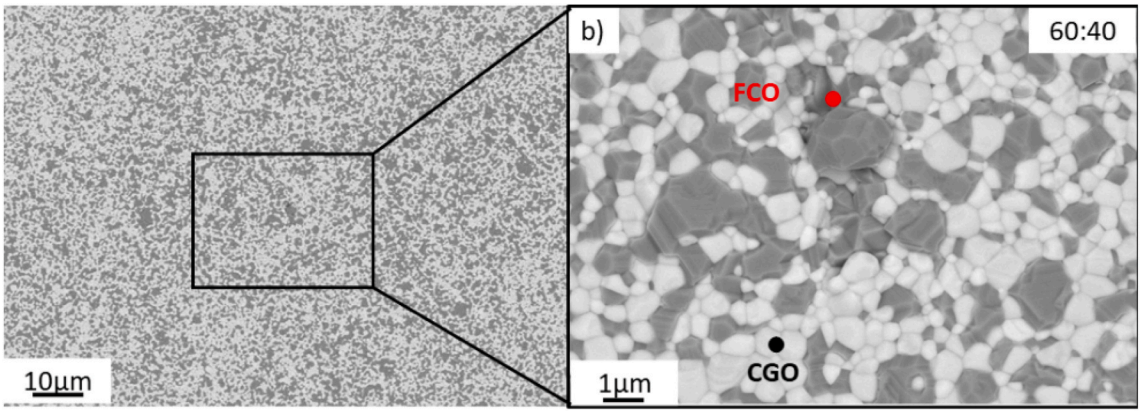

Fig. 6. SEM image of 60CGO10-FCO sintered at 1200 °C for 5h a) overview; b) detail with marked fluorite (light) and spinel (dark) grains.

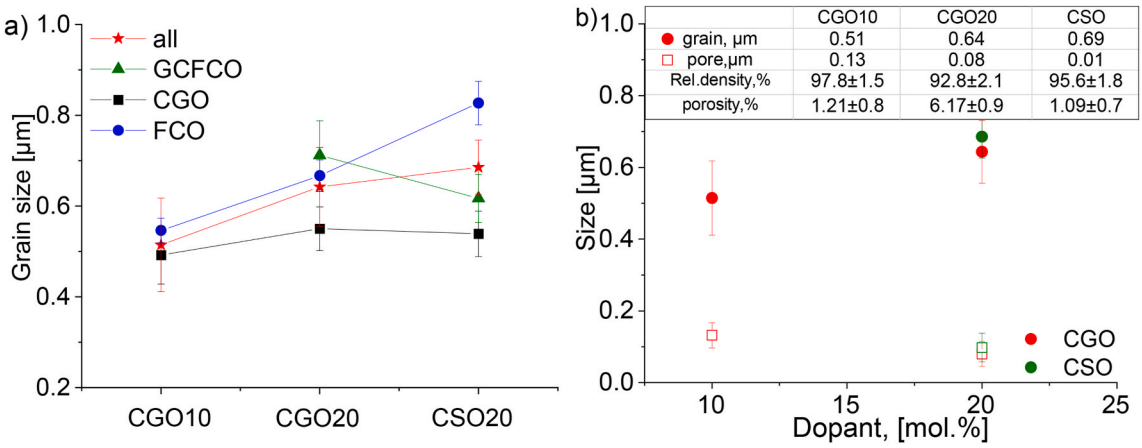

Fig. 7. a) Grain size of various phases in CGO10-, CGO20- and CSO20-based composites b) Grain and pore size relationship with the dopant fraction in the fluorite phase (solid lines for eye guidance only).

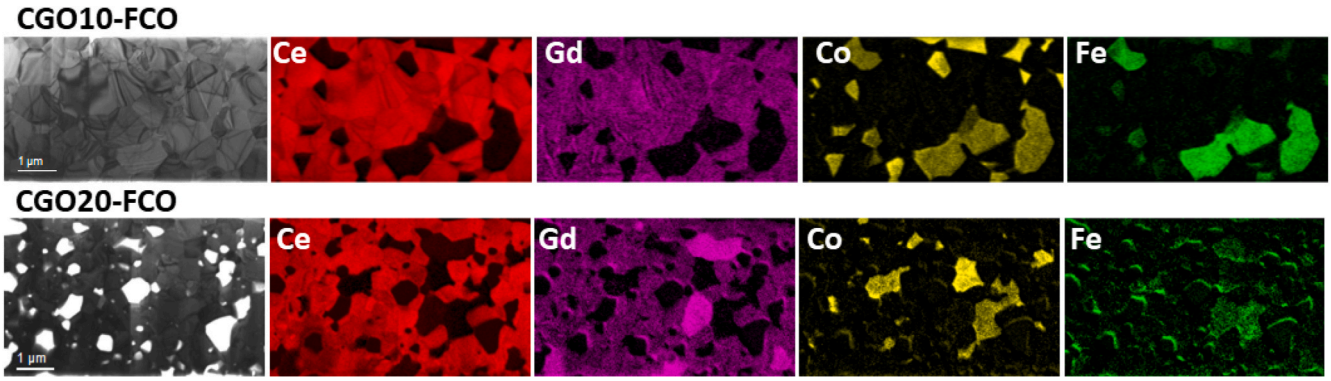

Fig. 8. Elemental mapping by TEM and EFTEM images of the CGO10-FCO and CGO20- FCO with ratio 60:40.

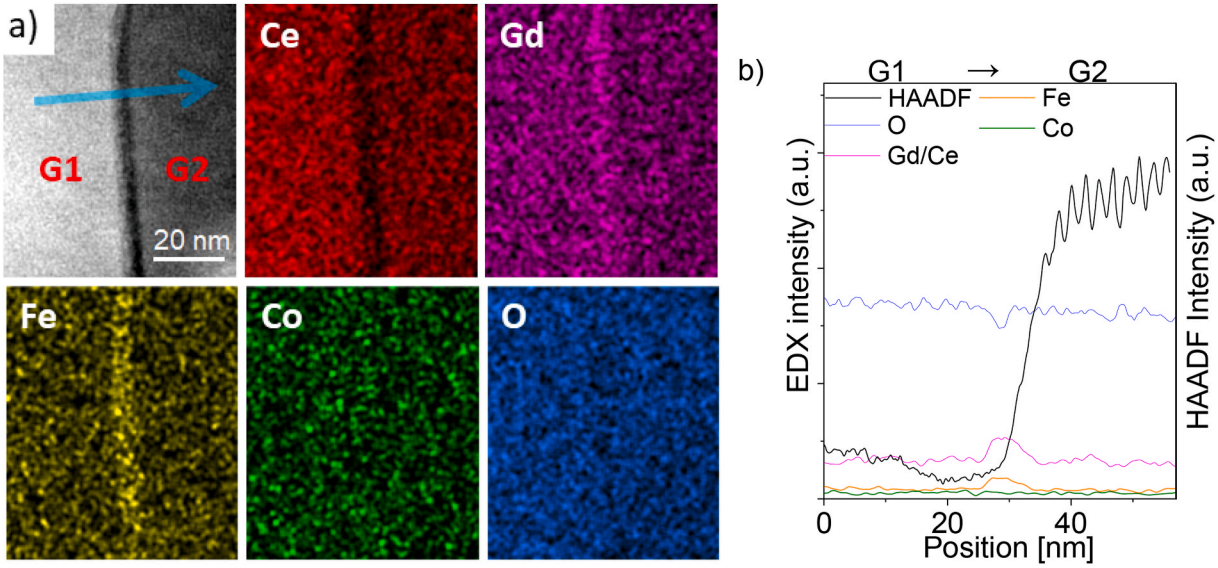

Fig. 9. EDXS analysis of the grain boundaries a) The simultaneously acquired HAADF image and EDXS chemical mapping from Ce L, Gd L, Fe K, Co K, and O K peak. b) Line scans between two fluorite grains marked as G1 and G2 based on the elemental maps.

performed by impedance spectroscopy in the temperature range of 400–800 °C. The ionic conductivity of the investigated materials is dominating in the entire temperature range in air; thus, electronic conductivity can be considered negligible. At 500 C the Sm-doped material shows the highest total conductivity followed by CGO10 and CGO20 as predicted by Koettgen et al. [35,37]. At higher temperatures, however, these differences disappear, which was also reported earlier [62,63].

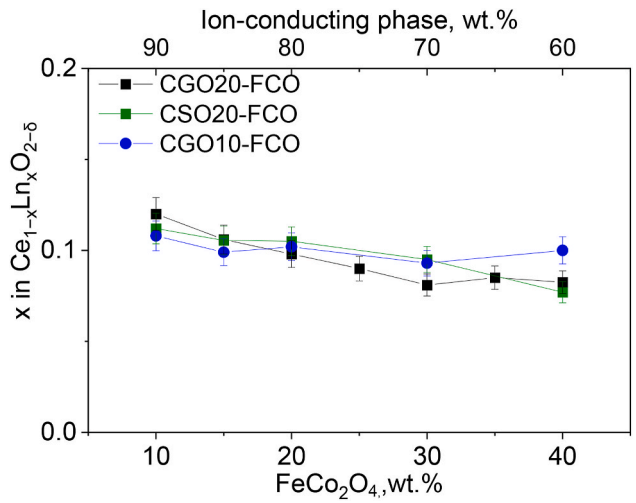

Fig. 10. Gd/Sm content in the fluorite phase of all investigated composites (solid lines for eye guidance only).

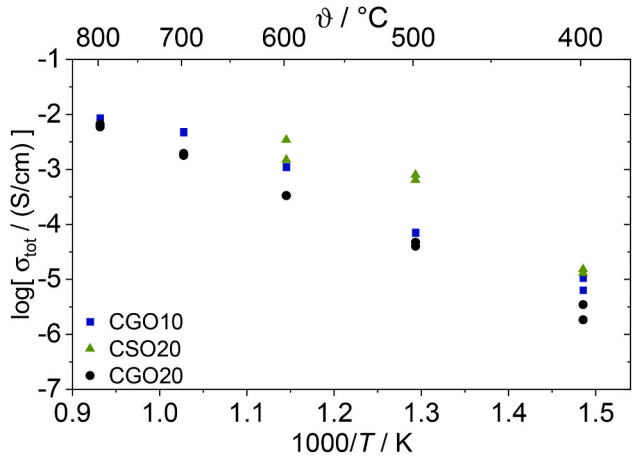

Fig. 11. Ion (total) conductivity of CGO20, CGO10, and CSO20 measured by impedance spectroscopy in a temperature range of 400–800 °C. Data for CSO20 was only obtained at temperature below 600 °C.

Fig. 12 a and b show the temperature dependent oxygen permeation rates and permeances of the composites with nominal fluorite-spinel wt. %-ratio of 60:40 and 80:20, respectively. The activation energies of thee composites (see Table 3) agree well with those of the ionic conductivity of doped ceria reported in literature ($E_{a\ CGO10}$ = 60–66 kJ/mol [29,43, 64], $E_{a\ CGO20}$ = 61–72 kJ/mol [29,43], $E_{a\ CSO20}$ = 74–94 kJ/mol [30,43, 62,65]), it is concluded that the ionic transport is rate limiting. As a consequence, the permeation rate increases with increasing ceria content in the composite. The data was measured after the permeation has reached a steady state. The maximum permeation rates were obtained with the 80:20 ratio at 1020 °C, i.e., 0.28, 0.26, and 0.22 ml/(cm^{2}min) for CGO10, CSO20, and CGO20, respectively. At lower temperatures, the activation energies slightly increase, which can be ascribed to an increasing contribution of oxygen surface exchange to the overall transport. Therefore, despite the LSCF coating, surface exchange can no longer be neglected for al composites.

The oxygen permeation of the three composites is evaluated as a function of the weight fraction of FCO (5 %-point-steps from 10 to 40 wt %) at 850 °C in Fig. 13 (left). Principally the performance of all composites reveals similar behavior along the investigated nominal FCO range. Starting from 40 wt % FCO the permeance increases with decreasing FCO content, revealing that ionic conductance is the rate limiting process. A maximum permeance is found at approximately 20 wt % nominal FCO for all three composites. A significant drop is seen in performance for all composites with 10 wt % of FCO probably due to lack of percolation in the electron conducting phases. However, due to phase interactions during sintering, the nominal weight fractions do not represent the actual volume fraction of the ionic and electronic conducting phases, respectively. Therefore, volume fractions were calculated from Rietveld-refined XRD-patterns as described in Ref. [19].

Fig. 13b shows that the maximum permeances of the different

Table 3
Activation energies E_a [kJ/mol] of the CGO10, CGO20 and CSO20-based composites at temperatures >800 °C calculated from permeances.

FCO wt.%	CSO20	CGO10	CGO20
10	103	102	101
15	76	66	74
20	79	68	58
25	-	-	60
30	78	75	62
35	-	–	80
40	95	74	80

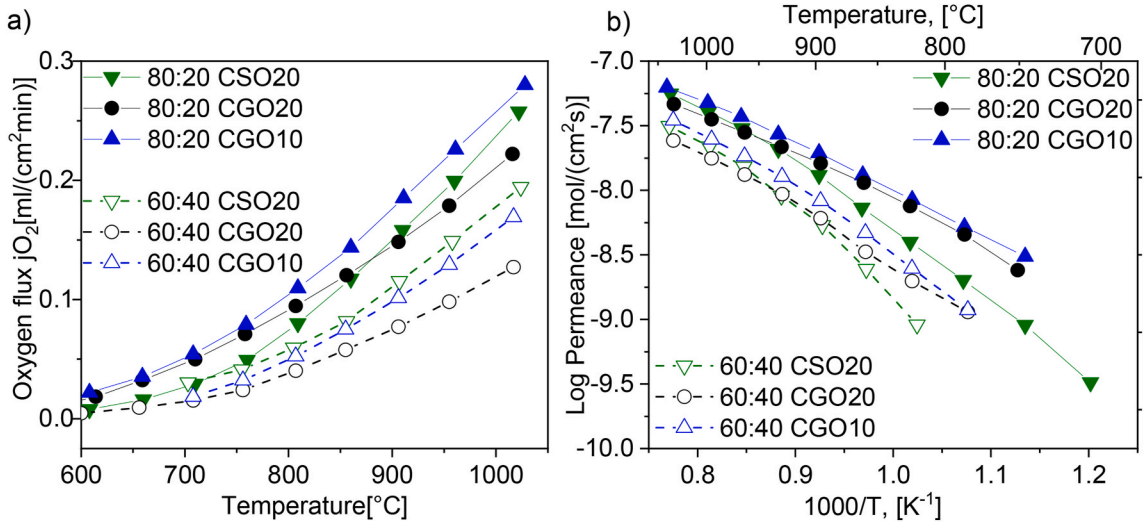

Fig. 12. Temperature dependence a) of the oxygen permeation flux and b) of the permeance of the ceria-based composites with 60:40 and 80:20 ratios (solid and dashed lines are a guide to the eye).

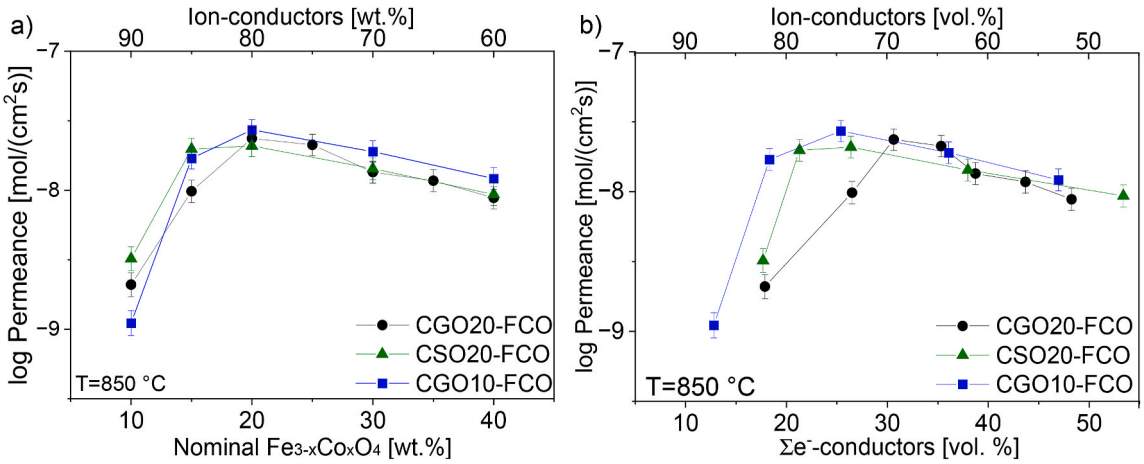

Fig. 13. a) Oxygen permeance as a function of the nominal spinel amount for the CSO20–FCO, CGO20- and CGO10-FCO composites synthesized by the SSRS technique at 850 °C; b) and as a function of the volume percentage of the electron conducting phase (solid lines for eye guidance only).

composites are achieved at very different volume fractions of electron conductors. This can be considered as percolation limit below which permeation decreases drastically due to the lack of electronic pathways. Obviously 20–30 vol% of electronic conducting phases are required for sufficient percolation marked as red dashed lines in Fig. 14, the percolation level varies with respect to the composite system [66,67]. Close to this percolation limit the permeance is presumably strongly dependent on the microstructure of the composite such as phase distribution and grain size. Moreover, the gadolinium, cobalt, and Iron enrichment along the grain boundaries might provide additional paths for the transport, affecting positively the percolation and final performance.

The better the compatibility, homogeneity, and uniformity of the phase distribution within the microstructure, the higher oxygen permeation is expected [68]. Similar results and the influence of components morphologies, such as grain size and morphology on performance are reported in Ref. [69], where it is concluded that a smaller grain size leads to a better percolation and, thus, oxygen permeation.

Based on our observation the microstructure features play a crucial role for the low amount of the electron conducting phase in the composite, especially under 25 wt % of the electron conducting phase in dual- and multi-phase composites. Now, the choice of the ion-conducting phase becomes relevant and strongly depends on the amount of the rare earth dopant. The dual-phase composite (10 mol.% of gadolinium) reveals no phase transformation, while in both 20 mol %-doped materials, the phase transformation takes place, resulting in a multi-phase structure. Although the formed perovskite phase in CGO20 and CSO20 is a pure electron conductor and contributes to the electronic transport, its conductivity is still not as high as it is for the FCO spinels [19]. The presence of stronger electron-conductor FCO might be more effective, than the mix of the FCO and GCFCO in the composite. Moreover, the transport across grain boundaries between FCO-GCFCO might be not as fast as that for FCO–FCO grain boundaries. Hence, it also can affect the transport process for charged particles.

4. Conclusion

MIEC composites based on commercially available powders of $Ce_{0.9}Gd_{0.1}O_{2-\delta}$ (CGO10) and $Ce_{0.8}Sm_{0.2}O_{2-\delta}$ (CSO20) in combination with spinel $FeCo_2O_4$ can be successfully synthesized by the cost-efficient solid-state reactive sintering (SSRS) technique. As a result, dense (~95 %) dual- and multi-phase materials with fine microstructure (0.5–0.7 μm) are produced for potential application in OTM. During the sintering process, several phase interactions occur in the CSO20–FCO composite resulting in a multiphase MIEC system, i.e., a cubic fluorite CSO, a cubic Fe/Co-spinel, and a donor-doped $SmFeO_3$ perovskite. In contrast, the composite CGO10-FCO reveals only two phases, i.e., a fluorite CGO10 and a Fe/Co-spinel, without the formation of tertiary phase, underlining the effect of the dopant amount (10 or 20 mol.%) in ceria. For both investigated in this study composites there was coexistence of two spinel types an iron-rich and a cobalt-rich spinel, according to the Fe–Co–O

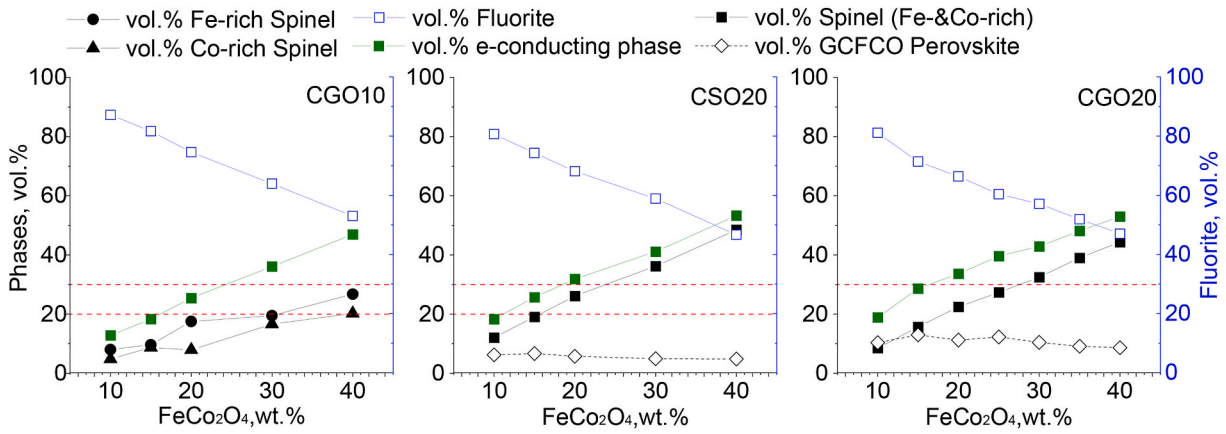

Fig. 14. Volume fraction of detected phases in the CGO10-, CGO20- and CSO20-based composites. Red dashed lines represent the region of effective percolation achieving high permeation rates (solid lines for eye guidance only). (For interpretation of the references to colour in this figure legend, the reader is referred to the Web version of this article.)

phase diagram.

The detected enrichment of gadolinium or samarium, cobalt, and ironalong grain boundaries impact the electronic or/and ionic transport and might enhance the total conductivity of the composite, resulting in high oxygen permeation of the dual- and multi-phase composites. This Fe/Co accumulation together with pre-existing Gd/Sm segregation at the grain boundaries possibly act as an initial state of the tertiary phase formation in 20 mol% doped ceria samples. However, in CGO10-based composites, the initial gadolinium fraction obviously is too low for the perovskite formation.

The main challenge of the dual-phase and multiphase materials design is maximizing the ionic conducting volume without losing the percolation of the electronic conduction. That's why to ensure sufficient percolating networks both conditions should be fulfilled: high electronic conductivity of the selected phases and continuous percolation paths for the transport. Investigated materials reveal an oxygen flux of 0.23 and 0.2 ml/(cm^2min) at 950 °C, for CGO10 and CSO20-based composites with 20 wt% of FCO phase, respectively. Based on our findings, the microstructure plays a major role in the low electron conducting phase content (<25 vol%) in the ceria-based composite, pointing out the importance of the phase distributions as well as the grain size of the presented phases. Thus, the CGO10-based composite has an advantage over the CGO20 and CSO20-based ones concerning the microstructure, resulting in higher oxygen permeance, particularly at low nominal FCO content. Microstructure-based modeling of the conductivity would be helpful in order to optimize the performance of such complex composite materials.

Author contributions

Liudmila Fischer: investigation & writing—original draft preparation, Kerstin Neuhaus: funding acquisition, investigation, project administration & writing – original draft, Christina Schmidt: investigation & writing—original draft preparation, Ke Ran: investigation & writing—original draft preparation, Patrick Behr: investigation, Stefan Baumann: conceptualization, investigation, funding acquisition & writing – original draft, Joachim Mayer: funding acquisition, & writing – review & editing, Henny J.M. Bouwmeester: conceptualization, Arian Nijmeijer: supervision & writing – review & editing, Oliver Guillon resources, supervision & writing – review & editing; Wilhelm A. Meulenberg: resources, supervision & writing – review & editing.

Funding

The work is funded by the Deutsche Forschungsgemeinschaft (DFG, German Research Foundation) – 387282673. Ke Ran acknowledges support by the Bundesministerium für Bildung und Forschung (NEUROTEC, 16ME0399, and 16ME0398K).

Declaration of competing interest

The authors declare the following financial interests/personal relationships which may be considered as potential competing interests:

Liudmila Fischer reports financial support was provided by Deutsche Forschungsgemeinschaft. Ke Ran, Kerstin Neuhaus, Christina Schmidt, Patrick Behr reports financial support was provided by Deutsche Forschungsgemeinschaft.

Ke Ran acknowledges support by the Bundesministerium für Bildung und Forschung (NEUROTEC, 16ME0399, and 16ME0398K).

Acknowledgments

Mr. S. Heinz for the assistances in lab works, sample preparations and permeation measurements, Ms Dr. D. Sebold for SEM and EDS investigations.

References

[1] W. Bai, J. Feng, C. Luo, P. Zhang, H. Wang, Y. Yang, Y. Zhao, H. Fan, A comprehensive review on oxygen transport membranes: development history, current status, and future directions, Int. J. Hydrogen Energy 46 (2021) 36257–36290.

[2] X. Dong, W. Jin, N. Xu, K. Li, Dense ceramic catalytic membranes and membrane reactors for energy and environmental applications, Chemical communications (Cambridge, England) 47 (2011) 10886–10902.

[3] X. Zhu, W. Yang, Microstructural and interfacial designs of oxygen-permeable membranes for oxygen separation and reaction-separation coupling, Adv. Mater. 31 (2019), e1902547.

[4] J. Garcia-Fayos, J.M. Serra, M.W. Luiten-Olieman, W.A. Meulenberg, Gas separation ceramic membranes, in: Advanced Ceramics for Energy Conversion and Storage, Elsevier, 2020, pp. 321–385.

[5] G. Chen, A. Feldhoff, A. Weidenkaff, C. Li, S. Liu, X. Zhu, J. Sunarso, K. Huang, X.-Y. Wu, A.F. Ghoniem, et al., Roadmap for sustainable mixed ionic-electronic conducting membranes, Adv. Funct. Mater. (2022) 32.

[6] R. Kiebach, S. Pirou, L. Martinez Aguilera, A.B. Haugen, A. Kaiser, P.V. Hendriksen, M. Balaguer, J. García-Fayos, J.M. Serra, F. Schulze-Küppers, et al., A review on dual-phase oxygen transport membranes: from fundamentals to commercial deployment, J. Mater. Chem. A 10 (2022) 2152–2195.

[7] A. Arratibel Plazaola, A. Cruellas Labella, Y. Liu, N. Badiola Porras, D. Pacheco Tanaka, M. Sint Annaland, F. Gallucci, Mixed ionic-electronic conducting membranes (MIEC) for their application in membrane reactors: a review, Processes 7 (2019) 128.

[8] J. Zhao, Y. Pang, C. Su, S. Jiang, L. Ge, Toward high performance mixed ionic and electronic conducting perovskite-based oxygen permeable membranes: an overview of strategies and rationales, Energy Fuels 37 (2023) 7042–7061.

[9] F. Drago, P. Fedeli, A. Cavaliere, A. Cammi, S. Passoni, R. Mereu, S. de La Pierre, F. Smeacetto, M. Ferraris, Development of a membrane module prototype for oxygen separation in industrial applications, Membranes 12 (2022).

[10] Q. Hu, S. Pirou, K. Engelbrecht, R. Kriegel, U. Pippardt, L. Kiesel, Q. Sun, R. Kiebach, Testing of high performance asymmetric tubular BSCF membranes under pressurized operation – a proof-of-concept study on a 7 tube module, J. Membr. Sci. 644 (2022), 120176.

[11] M.G. Sahini, B.S. Mwankemwa, N. Kanas, $Ba_xSr_{1-x}Co_yFe_{1-y}O_{3-\delta}$ (BSCF) mixed ionic-electronic conducting (MIEC) materials for oxygen separation membrane and SOFC applications: insights into processing, stability, and functional properties, Ceram. Int. 48 (2022) 2948–2964.

[12] J. Gao, L. Li, Z. Yin, J. Zhang, S. Lu, X. Tan, Poisoning effect of SO_2 on the oxygen permeation behavior of $La_{0.6}Sr_{0.4}Co_{0.2}Fe_{0.8}O_{3-\delta}$ perovskite hollow fiber membranes, J. Membr. Sci. 455 (2014) 341–348.

[13] J. Yi, M. Schroeder, High temperature degradation of $Ba_{0.5}Sr_{0.5}Co_{0.8}Fe_{0.2}O_{3-\delta}$ membranes in atmospheres containing concentrated carbon dioxide, J. Membr. Sci. 378 (2011) 163–170.

[14] D.N. Mueller, R.A. de Souza, T.E. Weirich, D. Roehrens, J. Mayer, M. Martin, A kinetic study of the decomposition of the cubic perovskite-type oxide $Ba_xSr_{1-x}Co_{0.8}Fe_{0.2}O_{3-\delta}$ (BSCF) (x = 0.1 and 0.5), Phys. Chem. Chem. Phys. : Phys. Chem. Chem. Phys. 12 (2010) 10320–10328.

[15] D. Matras, A. Vamvakeros, S.D.M. Jacques, V. Middelkoop, G. Vaughan, M. Agote Aran, R.J. Cernik, A.M. Beale, In situ X-ray diffraction computed tomography studies examining the thermal and chemical stabilities of working $Ba_{0.5}Sr_{0.5}Co_{0.8}Fe_{0.2}O_{3-\delta}$ membranes during oxidative coupling of methane, Phys. Chem. Chem. Phys. : Phys. Chem. Chem. Phys. 22 (2020) 18964–18975.

[16] A. Waindich, A. Möbius, M. Müller, Corrosion of $Ba_{1-x}Sr_xCo_{1-y}FeyO_{3-\delta}$ and $La_{0.3}Ba_{0.7}Co_{0.2}Fe_{0.8}O_{3-\delta}$ materials for oxygen separating membranes under Oxycoal conditions, J. Membr. Sci. 337 (2009) 182–187.

[17] T. Ramirez-Reina, J.L. Santos, N. García-Moncada, S. Ivanova, J.A. Odriozola, Development of robust mixed-conducting membranes with high permeability and stability, in: P. Granger, V.I. Parvulescu, W. Prellier (Eds.), Perovskites and Related Mixed Oxides, Wiley, 2016, pp. 719–738.

[18] M. Ramasamy, E.S. Persoon, S. Baumann, M. Schroeder, F. Schulze-Küppers, D. Görtz, R. Bhave, M. Bram, W.A. Meulenberg, Structural and chemical stability of high performance $Ce_{0.8}Gd_{0.2}O_{2-\delta}$ -$FeCo_2O_4$ dual phase oxygen transport membranes, J. Membr. Sci. 544 (2017) 278–286.

[19] L. Fischer, K. Neuhaus, C. Schmidt, K. Ran, P. Behr, S. Baumann, J. Mayer, W. A. Meulenberg, Phase formation and performance of solid state reactive sintered $Ce_{0.8}Gd_{0.2}O_{2-\delta}$ -$FeCo_2O_4$ composites, J. Mater. Chem. A 10 (2022) 2412–2420.

[20] Y. Lin, S. Fang, D. Su, K.S. Brinkman, F. Chen, Enhancing grain boundary ionic conductivity in mixed ionic-electronic conductors, Nat. Commun. 6 (2015) 6824.

[21] L. Fischer, K. Ran, C. Schmidt, K. Neuhaus, S. Baumann, P. Behr, J. Mayer, H.J. M. Bouwmeester, A. Nijmeijer, O. Guillon, et al., Role of Fe/Co ratio in dual phase $Ce_{0.8}Gd_{0.2}O_{2-}$ -$Fe_{3-x}Co_xO_4$ composites for oxygen separation, Membranes (2023) 13.

[22] F. Zeng, J. Malzbender, S. Baumann, M. Krüger, L. Winnubst, O. Guillon, W. A. Meulenberg, Phase and microstructural characterizations for $Ce_{0.8}Gd_{0.2}O_{2-\delta}$ -$FeCo_2O_4$ dual phase oxygen transport membranes, J. Eur. Ceram. Soc. 40 (2020) 5646–5652.

[23] C. Artini, M. Pani, M.M. Carnasciali, J.R. Plaisier, G.A. Costa, Lu-, Sm-, and Gd-doped ceria: a comparative approach to their structural properties, Inorg. Chem. 55 (2016) 10567–10579.

[24] C. Artini, M.M. Carnasciali, M. Viviani, S. Presto, J.R. Plaisier, G.A. Costa, M. Pani, Structural properties of Sm-doped ceria electrolytes at the fuel cell operating temperatures, Solid State Ionics 315 (2018) 85–91.

[25] H. Luo, K. Efimov, H. Jiang, A. Feldhoff, H. Wang, J. Caro, CO2-stable and cobalt-free dual-phase membrane for oxygen separation, Angew. Chem. 50 (2011) 759–763.

[26] H. Cheng, N. Zhang, X. Xiong, X. Lu, H. Zhao, S. Li, Z. Zhou, Synthesis, oxygen permeation, and CO_2 -tolerance properties of $Ce_{0.8}Gd_{0.2}O_{2-\delta}$ –$Ba_{0.95}La_{0.05}Fe_{1-x}Nb_xO_{3-\delta}$ dual-phase membranes, ACS Sustainable Chem. Eng. 3 (2015) 1982–1992.

[27] A.J. Samson, M. Søgaard, P. Vang Hendriksen, Gd Ce, O_2−-based dual phase membranes for oxygen separation, J. Membr. Sci. 470 (2014) 178–188.

[28] U. Nigge, Composites of Ce0.8Gd0.2O1.9 and Gd0.7Ca0.3CoO3−δ as oxygen permeable membranes for exhaust gas sensors, Solid State Ionics 146 (2002) 163–174.

[29] V.V. Kharton, F.M. Figueiredo, L. Navarro, E.N. Naumovich, A.V. Kovalevsky, A. A. Yaremchenko, A.P. Viskup, A. Carneiro, F.M.B. Marques, J.R. Frade, Ceria-based materials for solid oxide fuel cells, J. Mater. Sci. 36 (2001) 1105–1117.

[30] S. Presto, C. Artini, M. Pani, M.M. Carnasciali, S. Massardo, M. Viviani, Ionic conductivity and local structural features in $Ce_{1-x}Sm_xO_{2-x/2}$, Phys. Chem. Chem. Phys. : Phys. Chem. Chem. Phys. 20 (2018) 28338–28345.

[31] X. Zhu, H. Liu, Y. Cong, W. Yang, Novel dual-phase membranes for CO2 capture via an oxyfuel route, Chemical communications (Cambridge, England) 48 (2012) 251–253.

[32] J. Kilner, Fast oxygen transport in acceptor doped oxides, Solid State Ionics 129 (1–4) (2000) 13–23.

[33] M. Mogensen, Physical properties of mixed conductor solid oxide fuel cell anodes of doped CeO_2, J. Electrochem. Soc. 141 (1994) 2122.

[34] C. Artini, M. Viviani, S. Presto, S. Massardo, M.M. Carnasciali, L. Gigli, M. Pani, Correlations between structure, microstructure and ionic conductivity in (Gd,Sm)-doped ceria, Phys. Chem. Chem. Phys. : Phys. Chem. Chem. Phys. 24 (2022) 23622–23633.

[35] J. Koettgen, S. Grieshammer, P. Hein, B.O.H. Grope, M. Nakayama, M. Martin, Understanding the ionic conductivity maximum in doped ceria: trapping and blocking, Phys. Chem. Chem. Phys. : Phys. Chem. Chem. Phys. 20 (2018) 14291–14321.

[36] M. Coduri, S. Checchia, M. Longhi, D. Ceresoli, M. Scavini, Rare earth doped ceria: the complex connection between structure and properties, Front. Chem. 6 (2018) 526.

[37] J. Koettgen, M. Martin, The ionic conductivity of Sm-doped ceria, J. Am. Ceram. Soc. 103 (2020) 3776–3787.

[38] S. Wang, T. Kobayashi, M. Dokiya, T. Hashimoto, Electrical and ionic conductivity of Gd-doped ceria, J. Electrochem. Soc. 147 (2000) 3606.

[39] J.A. Kilner, R. Brook, A study of oxygen ion conductivity in doped non-stoichiometric oxides, Solid State Ionics 6 (1982) 237–252.

[40] J.H. Joo, G.S. Park, C.-Y. Yoo, J.H. Yu, Contribution of the surface exchange kinetics to the oxygen transport properties in $Ce_{0.9}Gd_{0.1}O_{2-\delta}$ –$La_{0.6}Sr_{0.4}Co_{0.2}Fe_{0.8}O_{3-\delta}$ dual-phase membrane, Solid State Ionics 253 (2013) 64–69.

[41] D. Gielen, M. Lyons, Critical Materials for the Energy Transition, Rare Earth elements, 2022.

[42] H.J. Avila-Paredes, K. Choi, C.-T. Chen, S. Kim, Dopant-concentration dependence of grain-boundary conductivity in ceria: a space-charge analysis, J. Mater. Chem. 19 (2009) 4837.

[43] B. Steele, Appraisal of $Ce_{1-y}Gd_yO_{2-y/2}$ electrolytes for IT-SOFC operation at 500°C, Solid State Ionics 129 (2000) 95–110.

[44] L. Malavasi, C.A.J. Fisher, M.S. Islam, Oxide-ion and proton conducting electrolyte materials for clean energy applications: structural and mechanistic features, Chem. Soc. Rev. 39 (2010) 4370–4387.

[45] Picture thresholding using an iterative selection method, IEEE Trans. Syst., Man, Cybern. 8 (1978) 630–632.

[46] A. Kovács, R. Schierholz, K. Tillmann, FEI titan G2 80-200 CREWLEY, JLSRF 2 (2016).

[47] H. Takamura, Y. Koshino, A. Kamegawa, M. Okada, Electrode and oxygen permeation properties of (Ce, Sm)O_2–MFe_2O_4 composite thin films (M=Co and Mn), Solid State Ionics 177 (2006) 2185–2189.

[48] M. Yousaf, N. Mushtaq, B. Zhu, B. Wang, M.N. Akhtar, A. Noor, M. Afzal, Electrochemical properties of $Ni_{0.4}Zn_{0.6}$ Fe_2O_4 and the heterostructure composites (Ni–Zn ferrite-SDC) for low temperature solid oxide fuel cell (LT-SOFC), Electrochim. Acta 331 (2020), 135349.

[49] A.N. Hansson, S. Linderoth, M. Mogensen, M.A. Somers, X-ray diffraction investigation of phase stability in the Co–Cr–O and the Fe–Co–Cr–O systems in air at 1323K, J. Alloys Compd. 402 (2005) 194–200.

[50] K. Neuhaus, R. Dolle, H.-D. Wiemhöfer, The effect of transition metal oxide addition on the conductivity of commercially available Gd-doped ceria, J. Electrochem. Soc. 167 (2020), 44507.

[51] Y. Ji, J. Kilner, M. Carolan, Electrical conductivity and oxygen transfer in gadolinia-doped ceria (CGO)–$Co_3O_{4-\delta}$ composites, J. Eur. Ceram. Soc. 24 (2004) 3613–3616.

[52] Y. Zheng, M. Zhou, L. Ge, S. Li, H. Chen, L. Guo, Effect of Fe2O3 on Sm-doped ceria system solid electrolyte for IT-SOFCs, J. Alloys Compd. 509 (2011) 546–550.

[53] T. Zhang, Iron oxide as an effective sintering aid and a grain boundary scavenger for ceria-based electrolytes, Solid State Ionics 167 (2004) 203–207.

[54] K. Ran, L. Fischer, S. Baumann, W.A. Meulenberg, K. Neuhaus, J. Mayer, Tuning the ceria interfaces inside the dual phase oxygen transport membranes, Acta Mater. 226 (2022), 117603.

[55] J.H. Joo, K.S. Yun, Y. Lee, J. Jung, C.-Y. Yoo, J.H. Yu, Dramatically enhanced oxygen fluxes in fluorite-rich dual-phase membrane by surface modification, Chem. Mater. 26 (2014) 4387–4394.

[56] S. Vives, D. Ramel, C. Meunier, Evolution of the structure with the composition and the defect arrangement in the gadolinium and samarium doped and co-doped ceria systems: a molecular dynamics study, Solid State Ionics 364 (2021), 115611.

[57] C.A. Schneider, W.S. Rasband, K.W. Eliceiri, NIH Image to ImageJ: 25 years of image analysis, Nat. Methods 9 (2012) 671–675.

[58] W.J. Bowman, J. Zhu, R. Sharma, P.A. Crozier, Electrical conductivity and grain boundary composition of Gd-doped and Gd/Pr co-doped ceria, Solid State Ionics 272 (2015) 9–17.

[59] W. Lee, H.J. Jung, M.H. Lee, Y.-B. Kim, J.S. Park, R. Sinclair, F.B. Prinz, Oxygen surface exchange at grain boundaries of oxide ion conductors, Adv. Funct. Mater. 22 (2012) 965–971.

[60] K. Ran, F. Zeng, L. Fischer, S. Baumann, W.A. Meulenberg, K. Neuhaus, J. Mayer, The in situ generated emerging phase inside dual phase oxygen transport membranes, Acta Mater. 234 (2022), 118034.

[61] Y. Lei, Y. Ito, N.D. Browning, T.J. Mazanec, Segregation effects at grain boundaries in fluorite-structured ceramics, J. Am. Ceram. Soc. 85 (2002) 2359–2363.

[62] K. Neuhaus, C. Schmidt, L. Fischer, W.A. Meulenberg, K. Ran, J. Mayer, S. Baumann, Measurement of polarization effects in dual-phase ceria-based oxygen permeation membranes using Kelvin probe force microscopy, Beilstein J. Nanotechnol. 12 (2021) 1380–1391.

[63] L.D. Jadhav, S.H. Pawar, M.G. Chourashiya, Effect of sintering temperature on structural and electrical properties of gadolinium doped ceria ($Ce_{0.9}Gd_{0.1}O_{1.95}$), Bull. Mater. Sci. 30 (2007) 97–100.

[64] S. Cheng, M. Søgaard, L. Han, W. Zhang, M. Chen, A. Kaiser, P.V. Hendriksen, A novel CO_2- and SO_2-tolerant dual phase composite membrane for oxygen separation, Chemical communications (Cambridge, England) 51 (2015) 7140–7143.

[65] H. Inaba, Ceria-based solid electrolytes, Solid State Ionics 83 (1996) 1–16.

[66] C.D. Lorenz, R.M. Ziff, Precise determination of the critical percolation threshold for the three-dimensional “Swiss cheese” model using a growth algorithm, J. Chem. Phys. 114 (2001) 3659–3661.

[67] B.T. Na, J.H. Park, J.H. Park, J.H. Yu, J.H. Joo, Elucidation of the oxygen surface kinetics in a coated dual-phase membrane for enhancing oxygen permeation flux, ACS Appl. Mater. Interfaces 9 (2017) 19917–19924.

[68] X. Zhu, H. Wang, W. Yang, Relationship between homogeneity and oxygen permeability of composite membranes, J. Membr. Sci. 309 (2008) 120–127.

[69] H. Luo, H. Jiang, K. Efimov, J. Caro, H. Wang, Influence of the preparation methods on the microstructure and oxygen permeability of a CO_2-stable dual phase membrane, AIChE J. 57 (2011) 2738–2745.